

## Research article

Yan Zuo<sup>a</sup>, Yerun Gao<sup>a</sup>, Shiyu Qin, Zhenye Wang, De Zhou, Zhen Li, Yu Yu\*, Ming Shao\* and Xinliang Zhang

# Broadband multi-wavelength optical sensing based on photothermal effect of 2D MXene films

<https://doi.org/10.1515/nanoph-2019-0338>

Received September 1, 2019; revised October 25, 2019; accepted November 2, 2019

**Keywords:** Mxene; integrated optics; multi-wavelength optical sensing; photothermal effect.

**Abstract:** Two-dimensional (2D) materials were widely used in sensing owing to the tunable physical or chemical properties. For years, optical sensing attracted a massive amount of attention on account of high accuracy, high security, non-invasive measurement, and strong anti-interference ability. Among the various optical sensing schemes, multi-wavelength optical sensing (MWOS) is an important branch and widely adopted in optical image, spectroscopy, or bio/chemical research. However, no spectral selectivity, limited working wavelength range, or intrinsic instability makes conventional 2D materials unsuitable for MWOS. A new class of 2D materials, known as MXene, exhibits outstanding electronic, optical, and thermal properties, leading to new applications in optical sensing. In this paper, we propose an integrated photothermal optical sensor (PHOS) using  $\text{Ti}_3\text{C}_2\text{T}_x$  MXene films. Thanks to the inherent spectral dependence of  $\text{Ti}_3\text{C}_2\text{T}_x$  MXene over a broadband range, the proposed PHOS can respond to different wavelengths from visible to short-wavelength infrared. Because of the efficient photothermal conversion, the PHOS has a control efficiency up to  $0.19 \pi \cdot \text{mW}^{-1} \cdot \text{mm}^{-1}$  under 980-nm laser pumping and shows a higher control efficiency under red light (690 nm) irradiation. The measured response time of the proposed PHOS is 23.4  $\mu\text{s}$ . This paper brings MXene into chip-integrated optical sensing fields for the first time and shows the potential applications.

## 1 Introduction

Two-dimensional (2D) materials have drawn tremendous interests due to the exceptional physical and chemical properties [1]. Moreover, some of these properties can be manipulated by temperature, pressure, light illumination, or electromagnetic field, making them good candidates for various sensing applications, ranging from physical, chemical to biological sensings [2, 3]. Among them, optical sensing, a kind of physical sensing, attracted much attention due to its high accuracy, high security, non-invasive measurement, and strong anti-interference ability [4, 5]. Benefitting from the rapid development of free space, fiber, and integrated optics, multifunctional optical sensors based on 2D materials were demonstrated successfully [6–10].

As different wavelengths can transmit diverse information, the multi-wavelength optical sensing (MWOS) exhibits superior performance [11, 12]. Unfortunately, conventional 2D materials encounter many difficulties in MWOS. Graphene, the first discovered 2D material, was used in sensing fields in many approaches [13, 14]. However, the flat absorption spectrum makes it insensitive to optical wavelength [15], which is not favored in MWOS. Although some assistant optical structures were constructed to respond to different wavelengths, the design and fabrication processes are complex and costly [16, 17]. Transition metal dichalcogenides (TMDs) are semiconductors with large bandgaps (1–2 eV), leading to a limited working wavelength range [18, 19]. Black phosphorus (BP), another typical 2D material, has a tunable bandgap (0.3–2 eV) and, thus, possesses different wavelength responses under different states [20, 21]. Nevertheless, the intrinsic instability hinders the applications. Other 2D materials, such as bismuthene [22, 23], are rarely reported in MWOS fields. Therefore, new materials with spectral

<sup>a</sup>Yan Zuo and Yerun Gao: These authors contributed equally to this work.

\*Corresponding authors: Yu Yu and Ming Shao, Wuhan National Laboratory for Optoelectronics, Huazhong University of Science and Technology, Wuhan 430074, China, e-mail: yuyu@mail.hust.edu.cn. <https://orcid.org/0000-0002-8421-6794> (Y. Yu); mingshao@hust.edu.cn (M. Shao)

Yan Zuo, Yerun Gao, Shiyu Qin, Zhenye Wang, De Zhou, Zhen Li and Xinliang Zhang: Wuhan National Laboratory for Optoelectronics, Huazhong University of Science and Technology, Wuhan 430074, China

sensitivity over a broadband wavelength range should be implanted to achieve MWOS with simple structures.

MXenes, a large family of transition metal carbides, nitrides and carbonitrides, are newly found 2D materials with rapid growing research interests [24].  $\text{Ti}_3\text{C}_2\text{T}_x$ , the most studied MXene, features many interesting properties such as high electrical conductivity, broadband nonlinear optical response, and plasmonic effect [25–27]. The optical absorption region of  $\text{Ti}_3\text{C}_2\text{T}_x$  covers from visible to short-wave infrared (SWIR) and shows strong wavelength dependence [28]. Moreover,  $\text{Ti}_3\text{C}_2\text{T}_x$  has an inherent high photothermal conversion efficiency in visible and near-infrared (NIR) regions [29], which means the absorbed light power can generate heat efficiently. Finally,  $\text{Ti}_3\text{C}_2\text{T}_x$  without any extra encapsulation can maintain a good stability in open air for about 1 month [25]. These unique properties make  $\text{Ti}_3\text{C}_2\text{T}_x$  MXene a fascinating candidate for MWOS.

In this work, for the first time, we incorporate  $\text{Ti}_3\text{C}_2\text{T}_x$  into the Mach-Zehnder interferometer (MZI) structure to construct a photothermal optical sensor (PHOS). Thanks to the efficient photothermal conversion of  $\text{Ti}_3\text{C}_2\text{T}_x$ , a controlling efficiency as high as  $0.19 \pi \cdot \text{mW}^{-1} \cdot \text{mm}^{-1}$  under 980-nm laser pumping can be obtained, and an even higher efficiency is observed under red light (690 nm) exposure. Owing to the wideband working wavelength of the  $\text{Ti}_3\text{C}_2\text{T}_x$  MXene films, the pumping wavelength of the proposed PHOS covers from visible to NIR light and can be further expanded to SWIR. The strong spectral sensitivity indicates that the proposed PHOS can respond to different wavelengths. The response time of the designed scheme is measured to be 23.4  $\mu\text{s}$ . This paper brings MXene into chip-integrated optical sensing, and it can find more applications in the areas of optical image, spectroscopy, or bio/chemical research.

## 2 Material preparation and characterization

The fabrication process of MXene colloidal solution is presented in Figure 1A. The  $\text{Ti}_3\text{AlC}_2$  power (97% purity, Laizhou Kai Kai Ceramic Materials Co., Ltd, China) was immersed in a mixed solution of 9 M hydrochloric acid (HCl, 20 ml, 36–38%, Sinopharm Chemical Reagent Co., Ltd, China) and lithium fluoride (LiF, 2 g, 0.08 mmol, 99.9%, Aladdin, China) at room temperature, followed by stirring for 24 h (1000 rpm) to remove the middle Al atomic layer. The resulting suspension was centrifuged (3500 rpm for 3 min) and then washed by deionized (DI) water several times

until  $\text{pH} > 4$ . The obtained solution was filtered using a 0.22- $\mu\text{m}$  membrane to get the multilayer  $\text{Ti}_3\text{C}_2\text{T}_x$  power. In the next step, we mixed  $\text{Ti}_3\text{C}_2\text{T}_x$  power and DI water in a ratio of 2:1. The suspension was then sonicated for 1 h and subsequently centrifuged at 3500 rpm for 1 h to acquire single- or few-layer flakes MXene. Finally, a colloidal solution was obtained for later spray coating.

We measured the conductivity of MXene in the air. The MXene film showed excellent electrical conductivity of 2000 S/cm, which is comparable to the values reported in literatures [25, 30]. Figure 1B and C represents the scanning electron microscopy (SEM) images of typical layer structures of delaminated  $\text{Ti}_3\text{C}_2\text{T}_x$  MXene under different magnifications. The SEM images reveal that exfoliated  $\text{Ti}_3\text{C}_2$  nanosheets are well stacked together. The AFM image, given in Figure 1D, reveals that large-area freestanding sheets with nanometer thickness can be created by the colloidal solution of single- or few-layer MXene.

The ultraviolet-visible-NIR (UV-vis-NIR) absorption spectrum of the synthesized  $\text{Ti}_3\text{C}_2\text{T}_x$  MXene films and colloidal solution are depicted in Figure 1E. Both MXene solution and films show strong absorption at visible range (400–500 nm), and the absorption band can be expanded to SWIR. Moreover, the absorbance under different film thicknesses and different polarization states were measured to provide a more comprehensive understanding (for details, see Supporting Material). From the results, the absorption is better under thick films, and the overall absorbance can be maintained above 60% when the thickness of the film reaches 671 nm. In terms of polarization, different linear polarization states are generated by a polarizer (LPVISE050-A, Thorlabs, Newton, NJ, USA), and the absorbance curves are almost identical under different conditions, indicating the isotropic nature of spray-deposited MXene films. To provide a more intuitive diagram, the absorbances at 600 nm are extracted and plotted in a polar coordinate (Figure S1C). The results illustrate that the polarization states have little influence on the absorption of MXene films.

The photothermal conversion efficiencies ( $\eta$ ) under different wavelengths were measured using the experimental setup shown in Figure 1F, which was taken by an IR camera (TI32, FLUKE, Everett, WA, USA). The real-time temperature of MXene colloidal solution with a concentration of 0.1 mg/ml can be read from the temperature profile depicted in Figure 1F. Photothermal heating and cooling curves under different wavelength laser irradiations are plotted in Figure 1G. According to a previous report, photothermal conversion efficiency ( $\eta$ ) is calculated by the following equation [29, 31]:

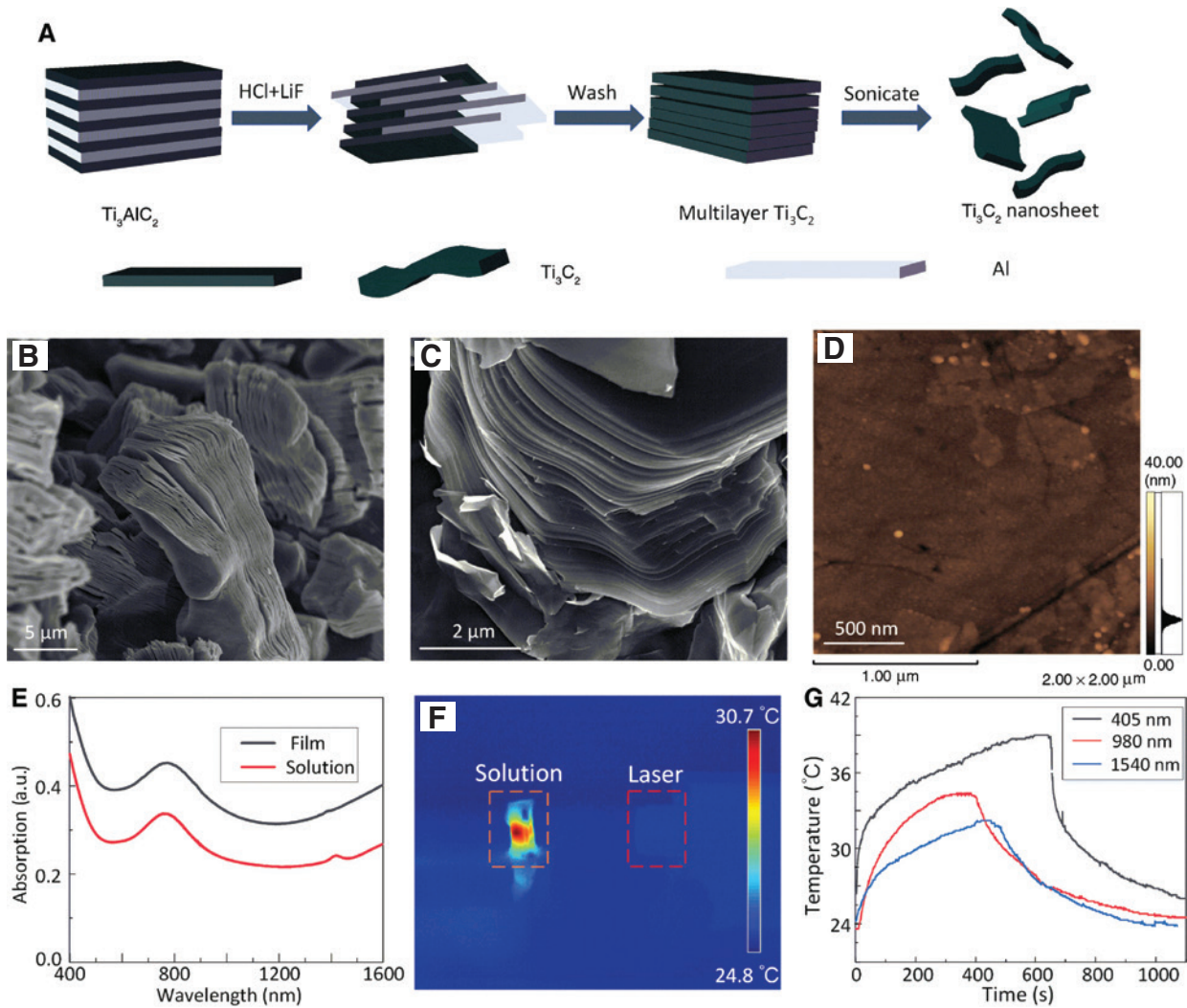


**Figure 1:** Preparation and characterization of the  $\text{Ti}_3\text{C}_2\text{T}_x$  MXene.

(A) The fabrication process of the  $\text{Ti}_3\text{C}_2\text{T}_x$  MXene. (B) and (C) SEM images of delaminated MXene sheets after etching under different magnifications. (D) The AFM image of exfoliated MXene sheet. (E) UV-vis-NIR absorption spectra of MXene film and 0.1-mg/ml colloidal solution. (F) Experimental setup and temperature profile for photo-thermal performance measurement. (G) Photothermal heating and cooling curves of  $\text{Ti}_3\text{C}_2\text{T}_x$  MXene upon exposure to different wavelength laser irradiances (405, 980, and 1540 nm).

$$\eta = \frac{hS(\Delta T_{\max, \text{mix}} - \Delta T_{\max, \text{H}_2\text{O}})}{P_{\text{in}}(1 - 10^{-A_{(\lambda)}})} \quad (1)$$

where  $h$  is the heat transfer coefficient of MXene,  $S$  is the surface area of the cell,  $\Delta T_{\max, \text{mix}}$  is the maximum temperature difference of the solution,  $\Delta T_{\max, \text{H}_2\text{O}}$  is the maximum temperature difference of DI water, and  $P_{\text{in}}$  is the laser power.  $A_{(\lambda)}$  represents the absorbance of the solution at a certain wavelength. The calculated  $\eta$  is near 100% at 405 nm, while  $\eta$  are 67% and 65.5% at 980 nm and 1540 nm, respectively. Compared with other reported 2D materials, the fabricated MXene shows advanced photothermal conversion efficiency (for details, see Supporting

Material). The final photothermal performance depends both on the light absorption performance and photothermal conversion efficiency. Therefore, owing to the strong absorption and high photothermal conversion efficiency, we consider  $\text{Ti}_3\text{C}_2\text{T}_x$  MXene as a good candidate for PHOS in MWOS fields.

### 3 Structure and principle

Figure 2A depicts the schematic of the proposed wavelength-sensitive PHOS, which is composed of two different lights. One is pumping light used for changing the



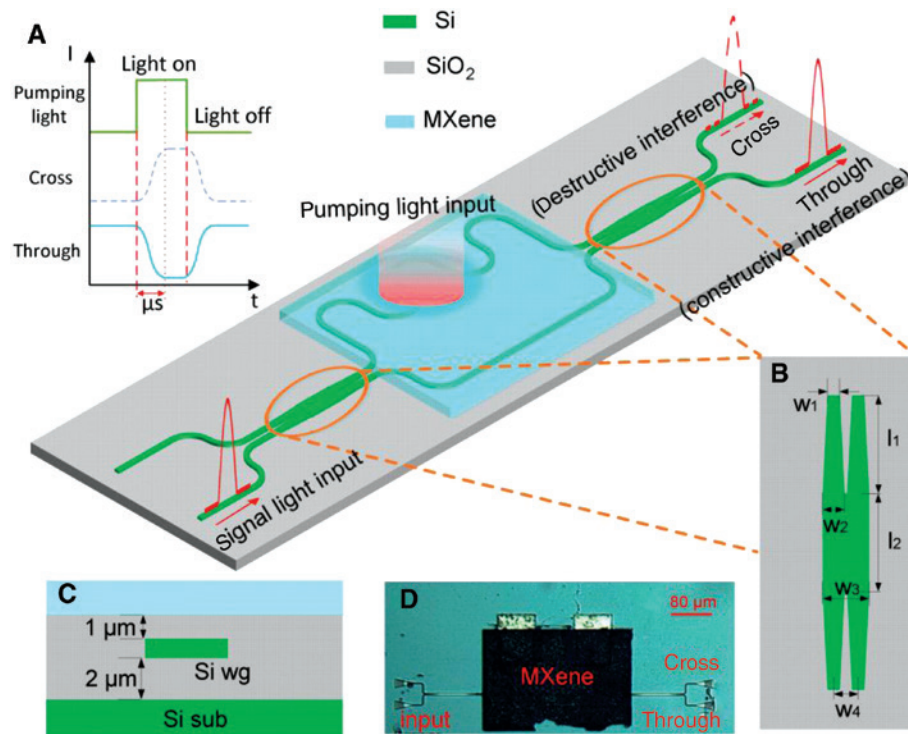


**Figure 2:** Schematic of the proposed PHOS.

(A) The whole structure is based on an SOI chip with two MMIs and an MZI. The  $\text{Ti}_3\text{C}_2\text{T}_x$  MXene films are deposited above the MZI. The signal light can come out from different ports under different pumping states. The inset shows the time response of the device. (B) Details of the MMI. (C) Cross section of the proposed PHOS. (D) Optical microscope image of the proposed PHOS. The whole MZI is under the  $\text{Ti}_3\text{C}_2\text{T}_x$  MXene films. Si wg, silicon waveguide; Si sub, silicon substrate.

properties of the material, which represents the variation of the surrounding media. The other is signal light used for detection. When the wavelength or intensity of the pumping light varies, the received power of the signal light will also change. Therefore, we can judge the state of the pumping light from the received signal light power, or we can control the propagation of the signal light by tuning the pumping light.

The signal light is guided in chip-integrated waveguides for the compact size. The whole structure is composed of two  $2 \times 2$  multimode interferences (MMIs) and an MZI. MMIs are used for splitting and combing signal lights, and the structure details are shown in Figure 2B with the following parameters:  $w_1 = 0.5 \mu\text{m}$ ,  $w_2 = 1.9 \mu\text{m}$ ,  $w_3 = 4 \mu\text{m}$ ,  $w_4 = 2.1 \mu\text{m}$ ,  $l_1 = 30 \mu\text{m}$ , and  $l_2 = 57.5 \mu\text{m}$ . The upper arm of the MZI adopts multiple-bending design to enhance the light-matter interaction, and the bending radius is  $10 \mu\text{m}$ , which is a tradeoff between modal loss and footprint. The whole structure is fabricated using deep UV lithography on a silicon-on-insulator (SOI) wafer with  $2 \mu\text{m}$  of buried oxide and  $220 \text{ nm}$  of top silicon. The cross section of the structure is shown in Figure 2C. The silicon strip waveguide with  $500\text{-nm}$  width and  $220\text{-nm}$  thickness is designed for single mode propagation. The

$\text{Ti}_3\text{C}_2\text{T}_x$  MXene films are deposited onto the MZI structure, and a  $1\text{-}\mu\text{m}$ -thick silicon oxide between the  $\text{Ti}_3\text{C}_2\text{T}_x$  MXene films and the waveguide is introduced to reduce the signal loss caused by the film absorption.

The MXene films are patterned on chip through UV lithography (for details, see Method), with a feature size of  $316 \times 215 \mu\text{m}^2$ . The film thickness is measured to be  $635 \text{ nm}$  by step profiler, which promises a high absorption of pumping light. The pumping light is vertically irradiated onto the MXene through an off-chip fiber. Figure 2D shows the microscope image of the fabricated device. The whole MZI is buried under the MXene films.

The working principle of MZI is based on dual beam interference, and the signal light can be exported from different ports depending on the pumping light states, as depicted in Figure 2A [32]. When the pumping light is on, the  $\text{Ti}_3\text{C}_2\text{T}_x$  MXene films absorb the pumping light and generate heat efficiently. The waveguide under the MXene films will be heated, and an extra phase shift is introduced due to the thermo-optic effect of the silicon. The signal light will come out from the through port once the extra phase shift offsets the phase difference introduced by the asymmetric structure, corresponding to a constructive interference. When the phase difference between

the two lights reaches  $\pi$  by changing either intensity or wavelength of the pumping light, the signal light will be exported from the cross port, corresponding to a destructive interference. Therefore, by tuning the pumping light states, we can get different outputs in the terminal. Moreover, benefiting from the compact size, the device can work in a microsecond time scale, as depicted in the inset of Figure 1A.

## 4 Device characterization and discussion

### 4.1 Wavelength-dependent control efficiency

Since  $\text{Ti}_3\text{C}_2\text{T}_x$  MXene films have different light absorptions and photothermal conversion efficiencies at different wavelengths, we first characterize the control efficiencies of PHOS under different wavelengths. Because of the difference between available pumping sources, the

experimental setups are not quite the same (for details, see Supporting Material). The signal/pumping lights are coupled into/onto the device through cleaved single mode fibers with a diameter of  $8.2\ \mu\text{m}$ . In this way, the pumping light can be fully utilized by adjusting the position of the coupling fiber. The corresponding results are shown in Figure 3A and B. Maximal phase shifts of  $7\pi$  and  $4.9\pi$  are obtained under pumping power of 400 mW at 980 and 1540 nm, respectively. After subtracting the coupling loss, the relationships between phase shifts and pumping powers at different wavelengths are plotted in Figure 3C. Linear slopes show the control efficiencies are 0.019 and  $0.012\ \pi/\text{mW}$ . Although the  $\text{Ti}_3\text{C}_2\text{T}_x$  MXene films cover the whole MZI, only a small area is under heating (decided by the modal size of the cleaved single mode fiber used for coupling), and the light-matter interaction length is around  $100\ \mu\text{m}$  (for details, see Supporting Material). After correcting the heating length, a control efficiency of  $0.19\ \pi \cdot \text{mW}^{-1} \cdot \text{mm}^{-1}$  under 980 nm pumping is obtained. Moreover, the signal wavelength is not limited in this range thanks to the broadband property of the on-chip elements.

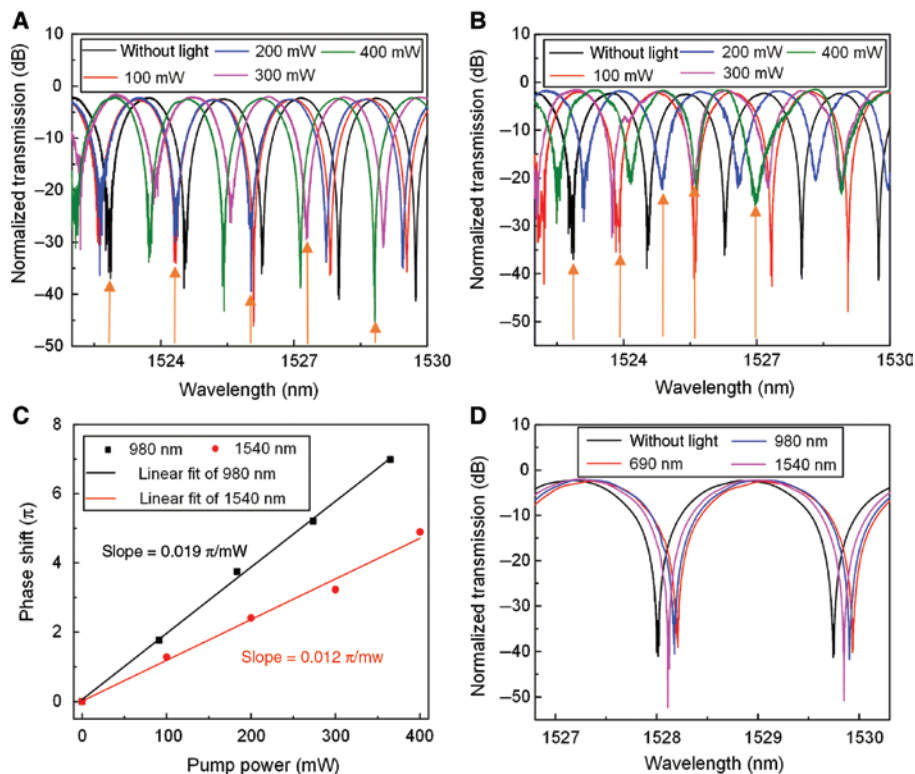


**Figure 3:** Static characterization of the proposed PHOS.

Normalized transmission spectra for different pumping powers under (A) 980-nm and (B) 1540-nm laser exposure. The orange arrows show the spectra shifts. (C) Measured and fitting phase shifts of 980-nm and 1540-nm pumping wavelengths as a function of the applied pumping power. (D) Measured and normalized transmission spectra for different pumping wavelengths. The pumping power is fixed at 10 mW.

The spectra upon the different pumping wavelengths at a fixed pumping power of 10 mW are compared in Figure 3D. The result shows a larger redshift under 690 nm light irradiation, due to higher light absorption and photothermal conversion efficiency of MXene in the visible range, corresponding to the above analysis. Because of the limitation of the available pumping source, only three pumping wavelengths are utilized. Considering the absorption range of the  $\text{Ti}_3\text{C}_2\text{T}_x$  MXene films, the working wavelength can be expanded to SWIR. This makes it competitive in MWOS.

## 4.2 Response time measurement

The response time of the proposed PHOS is further characterized using a modulated pumping light, while the signal wavelength is fixed at 1550 nm. Based on our available laser source that can be modulated, we set the pumping wavelength at 1540 nm, and the frequency of pumping light is set as 10 kHz. The modulated pumping light is recorded by a photodetector (KG-PR-200M-A, CONQUER, China) and an oscilloscope (RTM3000, ROHDE & SCHWARZ, Munich, Germany), and the waveform is plotted in Figure 4A. After that, the  $\text{Ti}_3\text{C}_2\text{T}_x$  MXene films are then heated by the modulated pumping light, and the output signal at the through port is monitored. The result is shown in Figure 4B. The rising and decaying edges are fitted with exponential functions of  $1 - \exp(-t/\tau_r)$  and  $\exp(-t/\tau_d)$ , respectively, as the red dash lines in Figure 4B indicated. The rise and decay times are estimated to be  $\tau_r = 23.4 \mu\text{s}$  and  $\tau_d = 5 \mu\text{s}$ . It is a phase reversal process. The fast decaying edge illustrates

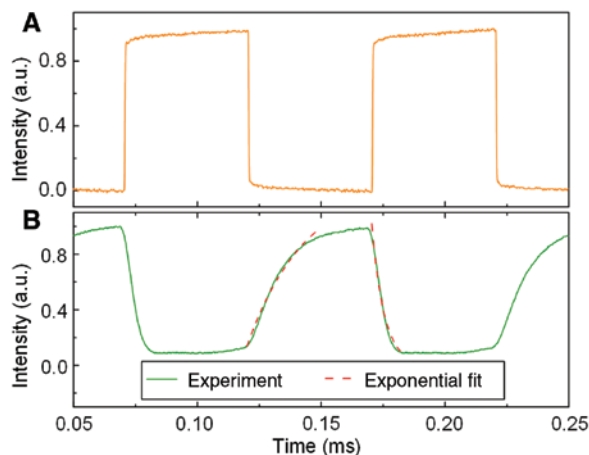


**Figure 4:** Dynamic response of the proposed PHOS. (A) The modulated pumping light and (B) corresponding temporal response signal. The frequency is set as 10 kHz. Red dash lines are the exponential fit of the rising and decaying edges.

that when the light heats the MXene, the signal light can rapidly be suppressed. It is a comprehensive process including heat generating by MXene and heat transport by the oxide. When the pumping light turns off, the relative slower rise time indicates a poor heat dissipation resulting from the low thermal conductivity of oxide.

## 4.3 Discussion

During the past years, MXene was widely used in optical and photonic areas, such as electromagnetic interference shielding [33], broadband mode-locking operation [34], broadband absorber [28], optical information converter [35], high-speed photodetector [36], and so on. All these applications indicate prominent optical properties of MXene. Following the steps, by exploiting the inherent wavelength dependence of MXene membrane, we bring it into MWOS with a simple integrated MZI structure. Figure 5A illustrates the working wavelength range of some typical 2D materials. The red dots and stars represent the pumping wavelengths used in the corresponding studies. The proposed PHOS can respond to different light irradiations from visible light to NIR and can be further

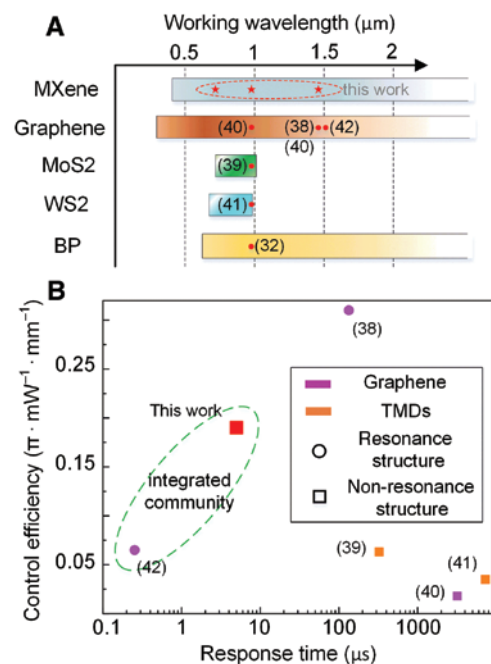


**Figure 5:** Comparison among different 2D materials. (A) The working wavelength of different 2D materials. The data of graphene, TMDs, and BP are taken from Refs. [15], [37], and [20], respectively. The red dots and stars represent the pumping wavelengths used in the corresponding literatures. (B) The control efficiency and response time of devices based on photothermal effect of different 2D materials.

expanded to SWIR, which is wider than that of TMDs. Moreover, the MXene films can overcome the difficulties in other 2D materials, including flat spectrum response in graphene and inherent instability in BP. All these merits make it a favorable material for MWOS. This work brings MXene into optical sensing fields and provides an alternative way to utilize MXene in photonic areas.

Thanks to the excellent photothermal conversion efficiency of MXene and the compact size of the device, the proposed PHOS also benefits in control efficiency and response time. Figure 5B compares the specifications of the reported devices based on photothermal effect of different 2D materials. The proposed PHOS shows a superior control efficiency that is one order of magnitude higher than that of most literatures reported. It also exhibits a superior response time that is two orders of magnitude faster compared to the PHOSs using non-integrated schemes [38–41]. In the integrated community, the higher control efficiency of the proposed PHOS means a more sensitive sensing, while the relatively slow response time can be improved using the same method in the reported literature [42], which deposited the 2D material on the waveguide directly.

Furthermore, inspired by the previous works, the control efficiency of the fabricated device can be improved from the following aspects: (i) Optimizing the position and size of the MXene films. As the large size will dissipate part of the energy and heat the two arms of the MZI simultaneously, the generated heat cannot be fully used for sensing. Optimizing the position and size of the MXene films is an efficient solution to improve the control efficiency. (ii) Adopting specific optical structure. To date, several optical structures, such as photonic crystal [43] and free-standing waveguides [44], were adopted to enhance the light-matter interaction, leading to power efficient optical devices. We expect to achieve a higher control efficiency after applying the above methods in the future work. The response time can be further improved by reducing the thickness of the silicon dioxide cladding layer between the MXene films and the silicon waveguide or replacing it with other materials possessing higher thermal conductivity.

## 5 Conclusion

In this paper, we fabricate a broadband MWOS with a simple structure by exploiting the inherent wideband response, spectral selectivity, and high photothermal conversion efficiency of MXene. The fabricated integrated PHOS has a high control efficiency of  $0.19 \pi \cdot \text{mW}^{-1} \cdot \text{mm}^{-1}$

under 980-nm laser pumping and a fast response time of 23.4  $\mu\text{s}$ . The proposed PHOS can also work under visible light pumping and show a higher tuning performance due to the higher absorption and photothermal conversion efficiency at specific wavelength range. This work brings MXene into optical sensing fields, and the proposed PHOS can be used in optical image, spectroscopy, or bio/chemical research.

## 6 Method

### 6.1 MXene film deposition

The SOI chip was first cleaned by acetone and absolute ethanol under bath sonication for 10 min, respectively. Photoresist (AZ5214) was then spin coated on the chip by a whirl glue device (1000 rpm for 5 s and 4000 rpm for 30 s). The chip was then heated under 97°C for 60 s and photolithographed using 1.5-s UV light exposure with a customized mask. A later 115°C for 90-s treatment was utilized to change the character of the photoresist, and 15-s UV light irradiation without mask was used for photolithography. The target area was developed by developing solution for 35 s and fixed by water for 20 s. Before spray coating, the chip was treated with ozone ( $\text{O}_3$ ) plasma for 5 min to remove the residual photoresist and enhance the adhesion of the oxide surface with MXene films. The synthesized MXene colloidal solution was sprayed onto the chip by an airbrush with 0.3-mm nozzle size and 0.1-MPa operating pressure. The airbrush was around 10 cm away from the chip and moved steadily to cover the whole chip, and a homogeneous thin film was obtained. After spray coating, the chip was immersed in acetone overnight and bath sonicated for 1 min to remove the excess MXene. Finally, the chip was dried in air for 30 min, and the whole device was completed.

## 7 Supplementary material

Supplementary Material is available online on the journal's website or from the author.

**Acknowledgment:** This work was financially supported by the National Nature Science Foundation of China (NSFC) (funder id: <http://dx.doi.org/10.13039/501100001809>, Grant Nos. 61922034, 61775073, and u1601651), Program for HUST Academic Frontier Youth Team (2018QYTD08), and Recruitment Program of Youth Experts of China.



## References

- [1] Tan C, Cao X, Wu X-J, et al. Recent advances in ultrathin two-dimensional nanomaterials. *Chem Rev* 2017;117: 6225–331.
- [2] Kannan PK, Late DJ, Morgan H, Rout CS. Recent developments in 2D layered inorganic nanomaterials for sensing. *Nanoscale* 2015;7:13293–312.
- [3] Varghese SS, Varghese SH, Swaminathan S, Singh KK, Mittal V. Two-dimensional materials for sensing: graphene and beyond. *Electronics* 2015;4:651–87.
- [4] Askim JR, Mahmoudi M, Suslick KS. Optical sensor arrays for chemical sensing: the optoelectronic nose. *Chem Soc Rev* 2013;42:8649–82.
- [5] Liu Y, Salemink HWM. All-optical on-chip sensor for high refractive index sensing. *Appl Phys Lett* 2015;106:031116.
- [6] Jin Z, Ye F, Zhang X, et al. Near-field coupled integrable two-dimensional InSe photosensor on optical fiber. *ACS Nano* 2018;12:12571–7.
- [7] Guo X, Hu H, Zhu X, Yang X, Dai Q. Higher order Fano graphene metamaterials for nanoscale optical sensing. *Nanoscale* 2017;9:14998–5004.
- [8] Nayeri M, Moradinasab M, Fathipour M. The transport and optical sensing properties of MoS<sub>2</sub>, MoSe<sub>2</sub>, WS<sub>2</sub> and WSe<sub>2</sub> semiconducting transition metal dichalcogenides. *Semicond Sci Technol* 2018;33:025002.
- [9] Xing F, Meng G-X, Zhang Q, et al. Ultrasensitive flow sensing of a single cell using graphene-based optical sensors. *Nano Lett* 2014;14:3563–9.
- [10] Vasic B, Gajic R. Graphene-covered photonic structures for optical chemical sensing. *Phys Rev Appl* 2015;4: 024007.
- [11] Chaudhary N, Khanuja M, Islam ASS. Hydrothermal synthesis of MoS<sub>2</sub> nanosheets for multiple wavelength optical sensing applications. *Sens Actuator A-Phys* 2018;277:190–8.
- [12] Diaz S. Stable dual-wavelength erbium fiber ring laser with optical feedback for remote sensing. *J Lightwave Technol* 2016;34:4591–5.
- [13] Justino CIL, Comes AR, Freitas AC, Duarte AC, Rocha-Santos TAP. Graphene based sensors and biosensors. *Trac-Trends Anal Chem* 2017;91:53–66.
- [14] Nag A, Mitra A, Mukhopadhyay SC. Graphene and its sensor-based applications: A review. *Sens Actuator A-Phys* 2018;270:177–94.
- [15] Bonaccorso F, Sun Z, Hasan T, Ferrari AC. Graphene photonics and optoelectronics. *Nat. Photonics* 2010;4:611–22.
- [16] Piper JR, Fan S. Total absorption in a graphene mono layer in the optical regime by critical coupling with a photonic crystal guided resonance. *ACS Photonics* 2014;1:347–53.
- [17] Liu Y, Cheng R, Liao L, et al. Plasmon resonance enhanced multicolour photodetection by graphene. *Nat Commun* 2011;2:579.
- [18] Mak KF, Shan J. Photonics and optoelectronics of 2D semiconductor transition metal dichalcogenides. *Nat Photonics* 2016;10:216–26.
- [19] Manzeli S, Ovchinnikov D, Pasquier D, Yazyev OV, Kis A. 2D transition metal dichalcogenides. *Nat Rev Mater* 2017;2:17033.
- [20] Castellanos-Gomez A. Black phosphorus: narrow gap, wide applications. *J Phys Chem Lett* 2015;6:4280–91.
- [21] Zheng J, Yang Z, Si C, et al. Black phosphorus based all-optical-signal-processing: toward high performances and enhanced stability. *ACS Photonics* 2017;4:1466–76.
- [22] Guo B, Wang SH, Wu ZX, et al. Sub-200 fs soliton mode-locked fiber laser based on bismuthene saturable absorber. *Opt. Express* 2018;26:22750–60.
- [23] Lu L, Wang W, Wu L, et al. All-optical switching of two continuous waves in few layer bismuthene based on spatial cross-phase modulation. *ACS Photonics* 2017;4:2852–61.
- [24] Anasori B, Lukatskaya MR, Gogotsi Y. 2D metal carbides and nitrides (MXenes) for energy storage. *Nat Rev Mater* 2017;2:16098.
- [25] Dillon AD, Ghidui MJ, Krick AL, et al. Highly conductive optical quality solution-processed films of 2D titanium carbide. *Adv Funct Mater* 2016;26:4162–8.
- [26] Michael N, Murat K, Volker P, et al. Two-dimensional nanocrystals produced by exfoliation of Ti<sub>3</sub>AlC<sub>2</sub>. *Adv Mater* 2011;23:4248–53.
- [27] Hantanasirisakul K, Zhao M-Q, Urbankowski P, et al. Fabrication of Ti<sub>3</sub>C<sub>2</sub>T<sub>x</sub> MXene transparent thin films with tunable optoelectronic properties. *Adv Electron Mater* 2016;2:1600050.
- [28] Chaudhuri K, Alhabeb M, Wang Z, Shalae VM, Gogotsi Y, Boltasseva A. Highly broadband absorber using plasmonic titanium carbide (MXene). *ACS Photonics* 2018;5:1115–22.
- [29] Li R, Zhang L, Shi L, Wang P. MXene Ti<sub>3</sub>C<sub>2</sub>: an effective 2D light-to-heat conversion material. *ACS Nano* 2017;11:3752–9.
- [30] Hantanasirisakul K, Gogotsi Y. Electronic and optical properties of 2D transition metal carbides and nitrides (MXenes). *Adv Mater* 2018;30:1804779.
- [31] Lin H, Wang X, Yu L, Chen Y, Shi J. Two-dimensional ultrathin MXene ceramic nanosheets for photothermal conversion. *Nano Lett* 2017;17:384–91.
- [32] Wang Y, Zhang F, Tang X, et al. All-optical phosphorene phase modulator with enhanced stability under ambient conditions. *Laser Photon Rev* 2018;12:1800016.
- [33] Shahzad F, Alhabeb M, Hatter CB, et al. Electromagnetic interference shielding with 2D transition metal carbides (MXenes). *Science* 2016;353:1137–40.
- [34] Jiang X, Liu S, Liang W, et al. Broadband nonlinear photonics in few-layer MXene Ti<sub>3</sub>C<sub>2</sub>T<sub>x</sub> (T = F, O, or OH). *Laser Photon Rev* 2018;12:1700229.
- [35] Wu L, Jiang X, Zhao J, et al. MXene-based nonlinear optical information converter for all-optical modulator and switcher. *Laser Photon Rev* 2018;12:1800215.
- [36] Kang Z, Ma Y, Tan X, et al. MXene–silicon van der Waals heterostructures for high-speed self-driven photodetectors. *Adv Electron Mater* 2017;3:1700165.
- [37] Wang QH, Kalantar-Zadeh K, Kis A, Coleman JN, Strano MS. Electronics and optoelectronics of two-dimensional transition metal dichalcogenides. *Nat Nanotechnol* 2012;7:699–712.
- [38] Wang Y, Gan X, Zhao C, et al. All-optical control of microfiber resonator by graphene's photothermal effect. *Appl Phys Lett* 2016;108:171905.
- [39] Wang Y, Wu K, Chen J. All-optical modulator based on MoS<sub>2</sub>-PVA thin film. *Chin Opt Lett* 2018;16:020003.
- [40] Yu L, Yin Y, Shi Y, Dai D, He S. Thermally tunable silicon photonic microdisk resonator with transparent graphene nanoheaters. *Optica* 2016;3:159–66.
- [41] Wu K, Guo C, Wang H, Zhang X, Wang J, Chen J. All-optical phase shifter and switch near 1550nm using tungsten disulfide (WS<sub>2</sub>) deposited tapered fiber. *Opt Express* 2017;25:17639–49.



- [42] Qiu C, Yang Y, Li C, Wu K, Chen J. All-optical control of light on a graphene-on-silicon nitride chip using thermo-optic effect. *Sci Rep* 2017;7:17046.
- [43] Yan S, Zhu X, Frandsen LH, et al. Slow-light-enhanced energy efficiency for graphene microheaters on silicon photonic crystal waveguides. *Nat Commun* 2017;8: 14411.
- [44] Dong P, Qian W, Liang H, et al. Thermally tunable silicon racetrack resonators with ultralow tuning power. *Opt Express* 2010;18:20298–304.

---

**Supplementary Material:** The online version of this article offers supplementary material (<https://doi.org/10.1515/nanoph-2019-0338>).